J Mol Model (2014) 20:2495
DOI 10.1007/s00894-014-2495-y

ORIGINAL PAPER

Interaction between phosphomolybdic anion and imidazolium cation in polyoxometalates-based ionic liquids: a quantum mechanics study

Yi Zheng · Jun Liu · Xiaoning Yang · Jun Wang

Received: 13 May 2014 / Accepted: 6 October 2014 / Published online: 25 October 2014

Abstract In this study, interaction between the phosphomolybdic anions ($[PMoO]^{3-}$) and 1-butyl-3-methyl imidazolium cations ($[Bmim]^{+}$) has been systematically studied by the density functional theory at the PBE-D3/TZP level. The stable geometries of the ion pairs with no imaginary frequencies were obtained and characterized. Multiple H-bonds formed between the cation and anion were revealed with the type of C-H···O. The interaction energy between the constituent $[PMoO]^{3-}$ anion and $[Bmim]^{+}$ cation is obviously larger than those in common ionic liquid. This is the possible reason for the relatively higher melting point of polyoxometalates (POMs)-based ionic liquids. It was observed that the interaction between the ion pairs was mainly contributed from the electrostatic interaction between $[PMoO]^{3-}$ and $[Bmim]^{+}$. The nature of the H-bonds was analyzed by the atoms in molecules (AIM) theory, harmonic vibrational frequency, the natural bond orbital (NBO), and the non-covalent interaction (NCI) approaches. The charge transfer and the orbital interaction between the ion pairs have also been identified, which may have an important influence on the electronic property of the ion pairs.

Keywords Density Functional Theory (DFT) · Imidazolium cations · Ionic liquids (ILs) · Phosphomolybdic anions · Polyoxometalate

Introduction

Ionic liquids (ILs) are a class of special compounds composed exclusively of organic cations and inorganic or organic anions. In general, ILs melt at relatively low temperatures (<100 °C) [1, 2]. ILs are considered to be green media owing to their low toxicity, low vapor pressure, absence of flammability, high thermal stability, negligible volatility, and so on. Furthermore, the physicochemical properties of ionic liquids could be adjusted through changing cation and anion [3]. It is such tunable properties that have led to the diverse applications of ILs as solvents and catalysts [4, 5]. However, for the common ILs, there exist some drawbacks [6], such as use of a large amount, relatively long reaction times, and difficulty in consequent separation.

In recent years, organic–inorganic hybrid materials have attracted considerable attention, because they possess the advantage of the flexible adaptability of both organic and inorganic groups [7]. Polyoxometalates (POMs) are metal-oxygen cluster anions of early transition metals with unmatched molecular structural diversity. There are widespread applications of POMs as acid and oxidation catalysts because of the controllable redox and acidic properties by the proper choice of constituent elements and counter cations [8, 9]. In addition, the polyoxometalate anions have been employed as the counter anions for ILs. Wang et al. [10] synthesized a series of POM salt catalysts containing the IL-cations, which were used as reaction-induced phase separation catalysts for the esterification reaction. The POM-based ILs have high melting temperature (above 100 °C) and are not the conventional ionic liquids [10]. They could be used as both homogeneous

Electronic supplementary material The online version of this article (doi:10.1007/s00894-014-2495-y) contains supplementary material, which is available to authorized users.

Y. Zheng · X. Yang (✉) · J. Wang
State Key Laboratory of Materials-Oriented Chemical Engineering, College of Chemistry and Chemical Engineering, Nanjing University of Technology, Nanjing 210009, China
e-mail: Yangxia@njtech.edu.cn

J. Liu
Fermitech (Beijing) Co. Ltd, Beijing 100085, China

catalysts with high efficiency, and heterogeneous catalysts, with easy recycle. At present, this POM-based catalysts, combining POM-anions and functionalized IL-cations, has been applied to various catalytic reactions, including esterification [10, 11], Beckmann rearrangement of ketoximes [12], oxidation of benzene alcohol [13], hydroxylation of benzene [14], oxidation of sulfides [15], oxidative desulfurization [16, 17], photo-polymerization [18], and so on. All these solid catalysts lead to liquid–solid heterogeneous catalytic systems, exhibiting not only high conversion and selectivity, but also convenient recovery and steady reuse.

In general, for these POM-based solid catalysts, the combination of POM anions and IL cations can be countless [19, 20]. The heterogeneous nature of the catalytic process is closely associated with the hydrogen bonding networks between anions and cations [10, 14]. The intramolecular charge transfer measured by UV–vis was also proposed to improve the redox property of POM-anions [15]. Although the POM anion is probably surrounded by several IL cations, the isolated ion pair is still the basic constituent ions in the POM-based ILs. In addition, in aqueous solution, the average coordination number of cations around the polyoxometallate Keggin anion is generally below one due to the solvation effect [21]. The contact between the anion and the neighbor cations does not follow the neutral matching. Therefore, the interaction between one POM anion and one organic cation is the fundamental aspect determining the property and performance of the POM-based ILs and its study is highly essential for the design and development of the materials.

The density functional theory (DFT) has been widely used for studying the molecular structure and electronic properties of various kinds of ILs [22, 23]. It has been found that the intermolecular interactions, including Coulombic force, hydrogen bond, and van der Waals interaction, have a significant effect on the structures and properties of different kinds of ILs [24–27]. However, the interaction between POM-anions and IL-cations has not been systematically studied, to our best knowledge. In this work, the interaction between the phosphomolybdic Keggin anion ($[PMoO]^{3-}$) and the 1-butyl-3-methyl imidazolium cation ($[Bmim]^{+}$) has been studied using the DFT method. The geometrical characteristics, electronic structures and interaction mechanism have been clarified. In particular, the formation of weak hydrogen bonds between the C-H groups on the imidazolium cation and the phosphomolybdic anion was identified.

Computational details

All the DFT calculations in this work were performed using the Amsterdam Density Functional (ADF) program [28]. We use the generalized gradient approximated (GGA) functional Perdew-Burke-Ernzerhof (PBE) [29] with the empirical dispersion correction (−D3) introduced by Grimme [30]. Triple-ζ plus polarization Slater basis sets (TZP) were employed for all atoms. The electrons from 1s to 3d shells for Mo and 1s to 2p for P have been treated by frozen core approximations in order to save the computation time without sacrificing the computation quality [31, 32], while all electron basis sets for the other atoms were used. Scalar relativistic effect for all atoms has been considered using the zero order regular approximation (ZORA) [33, 34]. Vibrational frequencies were calculated to verify the stationary structure for all the configurations. The interaction energies of the ion pairs are defined as follows:

$$\Delta E_{\text{int}} = E_{\text{ion pair}} - E_{\text{cation}} - E_{anion}. \quad (1)$$

The zero-point vibrational energy corrections (ZPE) were obtained within the harmonic approximation, and the basis set superposition errors (BSSE) were determined by means of the counterpoise correction of Boys and Bernardi [35]. The interaction energy can be further split up into four terms:

$$\Delta E_{\text{int}} = \Delta E_{elst} + \Delta E_{Pauli} + \Delta E_{oi} + \Delta E_{disp}, \quad (2)$$

where ΔE_{elst} corresponds to the classical electrostatic interaction between the unperturbed charge distributions of the prepared fragments. The Pauli repulsion ΔE_{Pauli} comprises the destabilizing interactions between the occupied orbitals and is responsible for steric repulsion. The orbital interaction energy ΔE_{oi} reflects electron pair bonding, charge transfer, and polarization [28]. The dispersion energy ΔE_{disp} is calculated using the empirical correction [30].

To analyze the nature of the interactions between the cation and anion, atoms in molecule (AIM) theory [36, 37], and natural bond orbital (NBO) [38] have also been calculated on the basis of optimized structures. Both of them are popular methods to study H-bonded systems and proved to be successful tools for interpreting H-bonding interactions. The reduced density gradient (RDG) function [39] in the non-covalent interaction (NCI) approach, which is an alternative but complementary method to AIM theory, has also been used to characterize the interactions.

Results and discussion

Geometrical features

The optimized structures of the isolated ions are displayed in Fig. 1, and the selected geometrical parameters of the stable geometry of $[Bmim]^{+}$ have been listed in Table 1. It is observed that the imidazolium ring exhibits a planar structure.

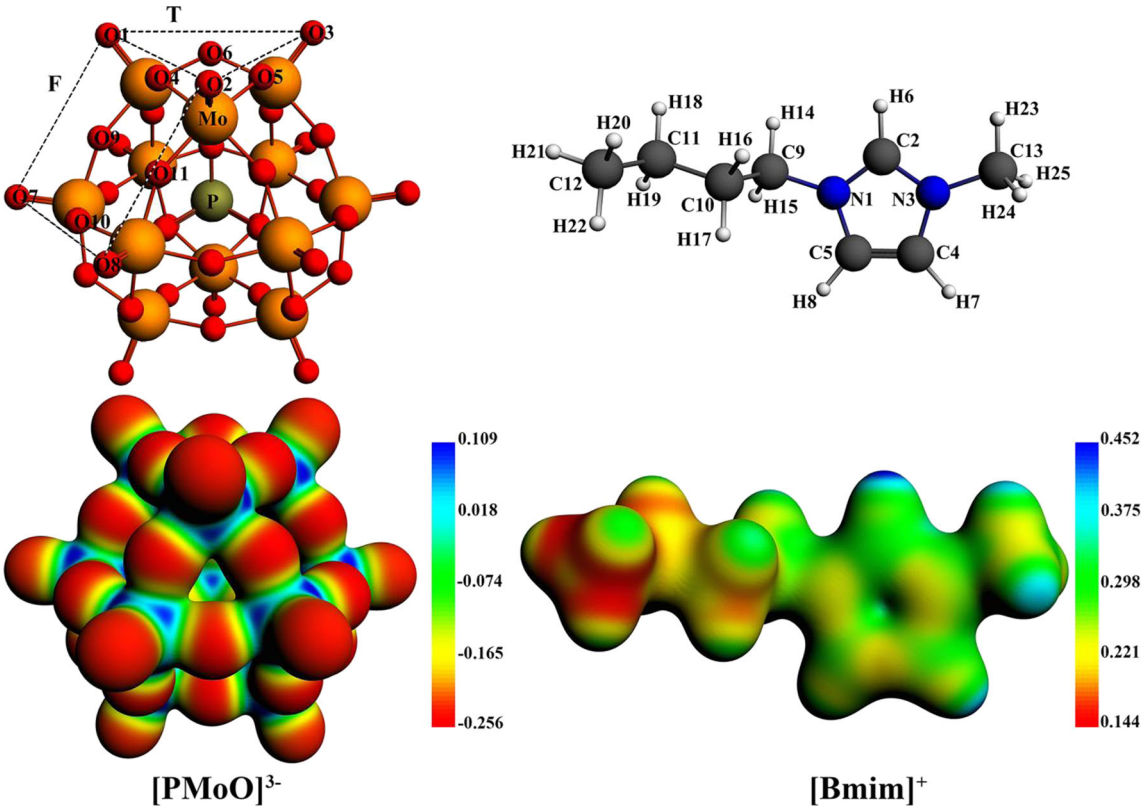

Fig. 1 The stable geometries of the isolated $[Bmim]^+$ cation and $[PMoO]^{3-}$ anion (upper panel). Their electrostatic potential surfaces are displayed below, where the red and blue identify regions of more negative and positive electrostatic potential, respectively. The isodensity contours are 0.03 electron $bohr^{-3}$. Based on the geometry of the anion, two regions are marked as T and F to represent two different interacting regions with the cation

The optimized geometries of $[PMoO]^{3-}$ agree very well with the experimental ones [40]. There are 40 oxygen atoms symmetrically arranged in the $[PMoO]^{3-}$ anion, classified into four types of oxygen: central oxygen atom bound to the phosphorus atom (O_a), terminal oxygen atom bound to a single molybdenum atom (O_d), corner-sharing oxygen atom which bridges two molybdenum atoms (O_b), and edge-sharing oxygen atom which bridges two molybdenum atoms and shares a central oxygen (O_c) [32]. Therefore, as shown in Fig. 1, O1, O2, O3, O7, and O8 are classified as O_d, while O4, O5, O6 as O_c, and O9, O10, O11 as O_b. The maximum deviations between the optimized structure and the experimental data are about 0.05 Å in the Mo-O_a and Mo-O_d bonds (see Table S1 in the electronic supplementary material). Similar discrepancy for the DFT optimization of other Keggin anions has been reported elsewhere [32, 41]

To obtain the possible interaction modes between the $[PMoO]^{3-}$ anion and the $[Bmim]^+$ cation, the electrostatic potential surfaces for the isolated ions have been constructed (bottom in Fig. 1). For the $[PMoO]^{3-}$ anion, the regions with more negative electrostatic potential for proton attack are around various oxygen atoms, which seem to have the same electrostatic potential. In fact, the bridging oxygen atoms possess more negative electrostatic potential than the terminal oxygen atoms (−0.246 au for O_b and −0.255 au for O_c vs −0.235 au for O_d), which is consistent with the previous study [42].

On account of the geometry of $[PMoO]^{3-}$ anion (T_d symmetry), two different regions are marked (Fig. 1): T region (connecting three terminal oxygen atoms, *i.e.*, O1, O2, and O3) and F region (connecting four terminal oxygen atoms, *i.e.*, O1, O2, O7, and O8). For the $[Bmim]^+$ cation, the C2-H6 group in the imidazolium ring shows more positive potential, as compared with the C4-H7 or C5-H8 groups. The hydrogen atoms in methyl group have more positive potential than those in butyl group.

In Fig. 2, six ion pair configurations, named as T1, T2, F1, F2, F3, and TF have been located during the DFT optimization processes. Configurations F3 and TF are consistent with the experimental X-ray crystal structures of 1-butyl-3-methyl imidazolium phosphomolybdate [40]. All the Cartesian coordinates of the geometries have been given in the electronic supplementary material. Additionally, during the geometry optimization, no stable configuration can be located for the interaction between the C4/C5-H of $[Bmim]^+$ and the oxygen atoms of $[PMoO]^{3-}$. This means the C4/C5-H is not the favorite site for the $[Bmim]^+$ cation to interact with the POM anion.

Table 1 The selected geometrical parameters of the $[Bmim]^+$ cation and six ion pairs

Parameters [a]	$[Bmim]^+$	T1	T2	F1	F2	F3	TF
N1-C2	1.342	1.343	1.341	1.346	1.346	1.341	1.341
C2-N3	1.344	1.345	1.341	1.344	1.344	1.341	1.341
N3-C4	1.383	1.382	1.382	1.382	1.383	1.383	1.386
C4-C5	1.368	1.365	1.368	1.366	1.367	1.386	1.365
C5-N1	1.383	1.383	1.384	1.381	1.383	1.382	1.387
C2-H6	1.084	1.09	1.087	1.095	1.101	1.084	1.093
C4-H7	1.084	1.083	1.083	1.083	1.083	1.082	1.082
C5-H8	1.084	1.082	1.083	1.082	1.083	1.084	1.083
N1-C9	1.478	1.471	1.469	1.474	1.476	1.468	1.472
C9-C10	1.528	1.525	1.526	1.525	1.525	1.527	1.529
C10-C11	1.533	1.532	1.532	1.531	1.534	1.532	1.532
C11-C12	1.53	1.53	1.53	1.529	1.53	1.53	1.529
C9-H14	1.098	1.097	1.096	1.098	1.096	1.095	1.098
C9-H15	1.098	1.099	1.098	1.096	1.101	1.097	1.101
C10-H16	1.103	1.103	1.104	1.102	1.099	1.104	1.1
C11-H18	1.103	1.102	1.103	1.101	1.102	1.102	1.104
C12-H20	1.1	1.101	1.102	1.1	1.1	1.102	1.098
N3-C13	1.467	1.464	1.462	1.465	1.467	1.464	1.465
C13-H23	1.094	1.096	1.094	1.095	1.095	1.096	1.095
C13-24	1.096	1.096	1.098	1.097	1.098	1.098	1.097
C13-25	1.096	1.096	1.096	1.097	1.096	1.096	1.097
$A_{N1-C2-N3}$	108.75	108.2	108.5	108.1	108.1	108.6	108.6
$A_{N3-C4-C5}$	107.02	107.2	107	107	107.1	107	107.1
$D_{N1-C2-N3-C4}$	−0.12	1.1	1.3	1.7	−0.2	0.8	−1.4
$D_{C2-N3-C4-C5}$	−0.12	−0.7	−0.6	−0.2	0.8	0.5	0.8

[a] A and D represent bond angle and dihedral angle. Distances are in angstroms and angles in degrees

As displayed in Fig. 2, the intermolecular H-bonds including the bond lengths and the corresponding bond angles are marked out, if the H···O distance is less than the van der Waals distance of 2.7 Å and the C-HO angle is greater than 90° [43]. The selected geometrical parameters of $[Bmim]^+$ cations in these ion pairs are also listed in Table 1. All optimized ion pairs have been characterized by multiple H-bonds formed between the electronegative oxygen atoms of $[PMoO]^{3-}$ anion and the C-H bonds of $[Bmim]^+$ cation. Our simulation provides a theoretical support to the previous experimental observation [40] of the H-bond formation between the phosphomolybdic anion and the C-H groups on the imidazolium cation. These H-bonds might form a network in the condensed phase ILs [10].

On average, the lengths of the H-bonds in the six configurations are shorter than the van der Waals H···O distance (2.7 Å) by about 15 %, implying that most of these C-H···O H-bonds are weak [44], which is different from those in common ILs [45]. It should be noted that for each configuration the C2-H6 group always involves in the formation of H-bond. In particular, the three H-bonds, the C2-H6···O4 (1.998 Å) in configuration F1, the C2-H6···O4 (1.874 Å) in configuration F2, and the C2-H6···O2 (2.017 Å) in configuration TF, are relatively shorter among all H-bonds, suggesting that the C2-H6 may be the most favorable site to form H-bond among the different C-H sites. As seen in Table 1, the C2-H6 bonds in the six configurations, except configuration F3, have been elongated more or less, whereas relatively less bond length change is observed for other C-H bonds.

In spite of the electrostatic potential difference of the edge-sharing oxygen atom O4 and the terminal oxygen atom O2, the H-bond lengths of the C2-H6···O4 in configuration T1 and the C2-H6···O2 in configuration T2 are nearly equal. Nevertheless, the H-bonds involving the C2-H6 and the edge-sharing oxygen atom O4 in configurations F1 and F2 are stronger than those involving the C2-H6 and the terminal oxygen atoms O1 or O2 in configurations F3 and TF. This indicates that strong H-bond could be formed with the edge-sharing oxygen atom in the F region. Configuration F1 has similar geometry with configuration F2, but their main

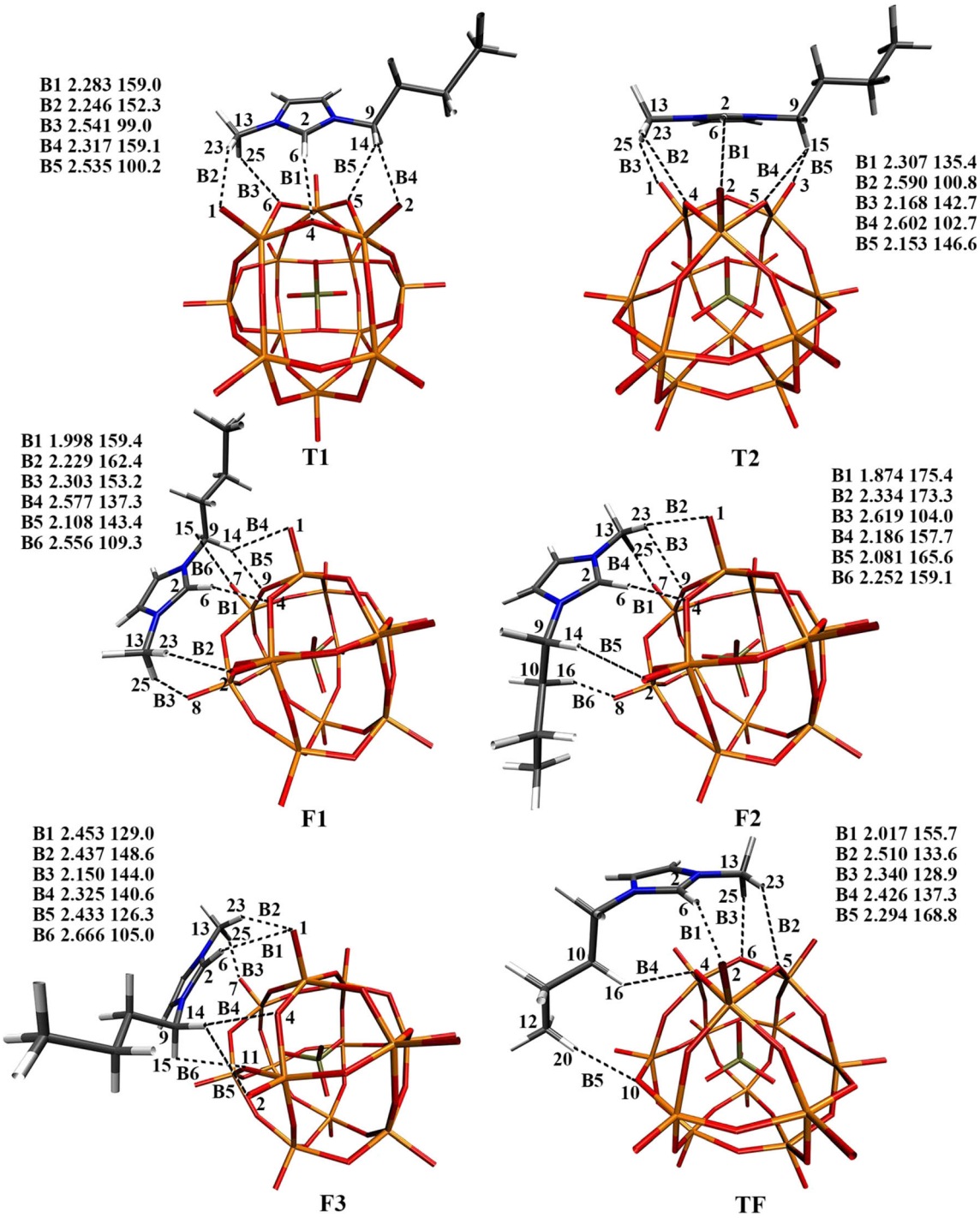

Fig. 2 Six optimized $[PMoO]^{3-}[Bmim]^{+}$ ion pairs at the PBE-D3/TZP level of DFT. All hydrogen bonds are indicated by dotted lines, and the corresponding bond lengths (in angstroms) and bond angles (in degrees) are listed for each configuration

difference is the orientation of the butyl group of $[Bmim]^{+}$ cation. In configuration TF, the imidazolium ring of $[Bmim]^{+}$ cation is above the edge-sharing oxygen atom O4 of $[PMoO]^{3-}$ anion, as a result, the H-bonds involve both T region and F region in the $[PMoO]^{3-}$ anion, which are different from other configurations.

The elongation of the C2-H6 bonds due to the formation of H-bond could be supported by the frequency shifts. Frequency analysis for all optimized structures shows no imaginary frequencies, advising that they are all minimum energy structures on the potential energy surface. As displayed in Fig. 3a, for the six ion pairs and the single $[Bmim]^{+}$ cation, the IR spectra are

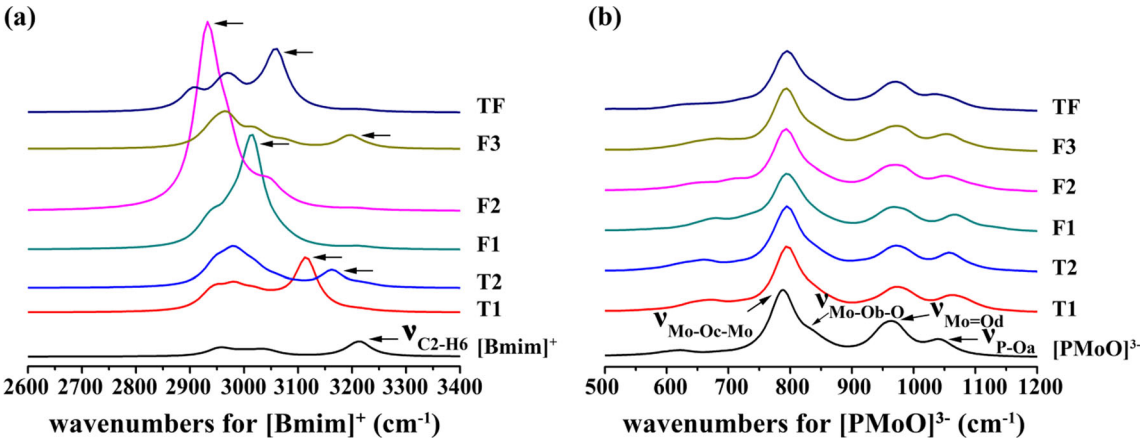

Fig. 3 Infrared spectra of the isolated ion and ion pairs. (**a**) The $[Bmim]^+$ cation in the isolated state and the ion pair states. (**b**) The $[PMoO]^{3-}$ anion in the isolated state and the ion pair states

mainly characterized by a strong absorption peak for the stretching vibration of the C2-H6 bond. In the isolated $[Bmim]^+$ cation, the absorption peak for the stretching vibration of the C2-H6 bond appears at about 3215 cm^{-1}. The largest red shift of 283 cm^{-1} of the C2-H6 stretching vibration is observed in configuration F2, corresponding to the strongest H-bond. The smallest red shifts of the C2-H6 stretching vibration in configurations T2 and F3 are less than 100 cm^{-1}. The magnitude of frequency shift for the C2-H6 bonds agrees with the trend of the C2-H6 bond elongation. Additionally, for the $[PMoO]^{3-}$ anion (Fig. 3b), the absorption peaks, assigned to the Keggin structure, occur at 1070 cm^{-1} for ν_{as} (P-Oa), 965 cm^{-1} for ν_{as} (Mo-Od), 870 cm^{-1} for ν_{as} (Mo-O-Mo), 790 cm^{-1} for ν_{as} (Mo-Oc-Mo), which are in good agreement with the experimental spectra of the $[PMoO]^{3-}$ anion [40]. The vibrational modes of the anion moiety from individual ion to ion pairs almost remain the same, implying the high structural stability of the $[PMoO]^{3-}$ anion.

Interaction energies

Table 2 lists the interaction energy ΔE_{int}, the interaction energy ΔE_C corrected by BSSE and ZPE, and the relative interaction energy ΔE_{CR}, along with the values of BSSE and ZPE at the PBE-D3/TZP level. For the six ion pairs, the interaction energies range from −169.25 to −161.37 kcal mol^{-1}, with the order of F1>F2≈F3>TF>T2>T1. This suggests that the ion pairs formed in the F region are more stable than those in the T region. Although configuration F1 is more stable than configuration F2, the H-bond, C2-H6···O4, in configuration F2, is the strongest one among all H-bonds. Configuration F3 has similar energetic stability with F2, but the H-bond C2-H6···O1 in configuration F3 is weaker. Configuration TF has the intermediate stability among the six configurations. From the energetic analysis, the experimentally observed configurations, F3 and TF, are not the most stable. This could be ascribed to the additional effect of the surrounding environment in the experimental solid state condition [46, 47].

In our IL system with the $[PMoO]^{3-}$ anion and the $[Bmim]^+$ cation, the interaction energy between the cation and the anion is obviously larger than those in common ILs [48–50]. The larger interaction energy might lead to the solid nature of this POM-based ILs. To understand the origin of the interaction between the $[Bmim]^+$ and $[PMoO]^{3-}$, we employed the energy decomposition analysis [51–53] to evaluate the various energetic contributions. Table 3 presents the

Table 2 The interaction energies (in kcal mol^{-1}) of six ion pairs

Ion pairs	ΔBSSE[a]	ΔZPE[a]	ΔE_{int} [a]	ΔE_C [a]	ΔE_{CR} [a]
T1	1.70	1.62	−164.69	−161.37	7.88
T2	1.85	1.49	−165.68	−162.34	6.91
F1	2.03	1.83	−173.11	−169.25	0.00
F2	2.05	1.51	−171.46	−167.90	1.35
F3	2.02	1.38	−171.39	−167.99	1.26
TF	2.19	0.79	−169.00	−166.02	3.23

[a] ΔBSSE, ΔZPE, ΔE_{int}, ΔE_C, and ΔE_{CR} represent the values of BSSE, ZPE, the interaction energies, the interaction energies corrected by BSSE and ZPE, and the relative interaction energies

Table 3 Energy decomposition of interaction energies (in kcal mol^{-1}) for six ion pairs

Ion pairs	ΔE_{elst}	ΔE_{Pauli}	ΔE_{oi}	ΔE_{disp}
T1	−153.04	25.01	−26.33	−10.33
T2	−156.35	26.55	−24.69	−11.19
F1	−160.83	30.23	−29.52	−12.98
F2	−159.88	33.52	−32.48	−12.62
F3	−160.45	27.54	−25.15	−13.33
TF	−158.84	31.84	−28.22	−13.77

energy decompositions for all configurations. The electrostatic attraction energy accounts for more than 90 % of the total interaction energy, whereas the dispersion energy only contributes less than 10 %. The electrostatic attraction energy is the dominant contribution to the interaction energy [24]. Although the larger electrostatic interaction between the PMoO anion and the counter-ion (IL cation) is associated with the high negative charge (−3) in the anion, it definitely reflects the Coulombic attraction between the constituent ions in the condensed-phase $[Bmim]^{+}_{3}[PMoO]^{3-}$ ionic liquid, consequently leading to a larger lattice energy. This result confirms the previous experimental observation that Coulombic attraction between ion pairs is responsible for the crystalline lattice state of POM-based ILs with higher melting points [54, 55].

It is noted that in configurations F1, F2, F3, and TF, the difference in the interaction energies is due to the Pauli

Table 4 Properties of the electron density (in au) at bond critical points for the intermolecular interaction of six ion pairs

Ion pairs	BCP	ρ	λ_1	λ_2	λ_3	$\nabla^2\rho$
T1	C2-H6···O4	0.0128	−0.0129	−0.0122	0.0706	0.0455
	C13-H23···O	0.0140	−0.0149	−0.0140	0.0795	0.0505
	C13-H25···O6	0.0111	−0.0088	−0.0049	0.0594	0.0457
	C9-H14···O2	0.0121	−0.0124	−0.0112	0.0672	0.0435
	C9-H14···O5	0.0112	−0.0091	−0.0042	0.0597	0.0464
T2	C2-H6···O2	0.0129	−0.0134	−0.0116	0.0714	0.0464
	C13-H23···O4	0.0097	−0.0073	−0.0048	0.0519	0.0398
	C13-H25···O1	0.0171	−0.0190	−0.0183	0.0988	0.0616
	C9-H15···O3	0.0179	−0.0198	−0.0191	0.1027	0.0638
	C9-H15···O5	0.0094	−0.0069	−0.0040	0.0497	0.0389
F1	C2-H6···O4	0.0248	−0.0317	−0.0313	0.1454	0.0824
	C13-H23···O2	0.0138	−0.0146	−0.0134	0.0777	0.0497
	C13-H25···O8	0.0117	−0.0119	−0.0110	0.0653	0.0423
	C9-H14···O1	0.0079	−0.0068	−0.0024	0.0388	0.0296
	C9-H14···O9	0.0203	−0.0230	−0.0217	0.1164	0.0717
	C9-H15···O7	0.0091	−0.0079	−0.0054	0.0493	0.0360
	C11-H18···O1	0.0057	−0.0047	−0.0044	0.0297	0.0206
F2	C2-H6···O4	0.0315	−0.0443	−0.0435	0.1879	0.1001
	C13-H23···O1	0.0112	−0.0114	−0.0104	0.0625	0.0407
	C13-H23···O9	0.0092	−0.0077	−0.0039	0.0479	0.0362
	C13-H25···O7	0.0158	−0.0177	−0.0165	0.0911	0.0568
	C9-H14···O2	0.0200	−0.0238	−0.0225	0.1173	0.0710
	C10-H16···O11	0.0052	−0.0040	−0.0014	0.0251	0.0198
	C10-H16···O8	0.0136	−0.0144	−0.0138	0.0780	0.0498
	C11-H18···O2	0.0066	−0.0055	−0.0047	0.0339	0.0238
	C12-H20···O8	0.0055	−0.0046	−0.0040	0.0289	0.0202
F3	C2-H6···O1	0.0102	−0.0090	−0.0073	0.0539	0.0376
	C13-H23···O1	0.0095	−0.0088	−0.0086	0.0515	0.0342
	C13-H25···O7	0.0176	−0.0197	−0.0192	0.1023	0.0634
	C9-H14···O4	0.0128	−0.0127	−0.0112	0.0702	0.0464
	C9-H14···O2	0.0110	−0.0095	−0.0079	0.0585	0.0411
	C9-H15···O11	0.0080	−0.0063	−0.0039	0.0419	0.0317
	C11-H18···O2	0.0036	−0.0023	−0.0017	0.0173	0.0132
TF	C2-H6···O2	0.0232	−0.0289	−0.0269	0.1351	0.0793
	C13-H23···O5	0.0089	−0.0081	−0.0074	0.0473	0.0317
	C13-H24···O6	$0.0127E^{(2)}$	−0.0127	−0.0119	0.0709	0.0463
	C10-H16···O4	0.0105	−0.0097	−0.0095	0.0572	0.0380
	C10-H16···O9	0.0051	−0.0039	−0.0022	0.0257	0.0197
	C12-H20···O10	0.0126	−0.0132	−0.0127	0.0713	0.0454

repulsion and orbital interaction. For example, configuration F2 has the largest orbital interaction energy, which is consistent with the strongest H-bond C2-H6···O4. The orbital interaction in the six ion pairs can be further analyzed by the ETS-NOCV scheme [56, 57], which combines the extended transition state (ETS) approach with the natural orbitals for chemical valence (NOCV) method. The important function of the NOCV analysis can be applied to clarify which H-bond has the main contribution to the orbital interaction in each ion pair. The detailed results for all six ion pair configurations are presented in Fig. S1 in the supplementary material. For all the NOCV decompositions in the six ion pair configurations, each energy contribution term is very small. This is consistent with the weak H-bonding nature in this system. For instance, for configuration F2, the maximum energy contribution (ΔE=−5.915 kcal mol^{-1}) to the orbital interaction comes from the donation from the occupied O4 long-pair orbital to the C2-H6 virtual orbital, which represents the contribution from the C2-H6···O4 H-bonding. This is consistent with the preceding geometrical result that the C2-H6 group always involves the H-bond formation. The second larger contribution to the orbital energy is from the H-bond of C9-H15···O7 with the energy ΔE=−2.399 kcal mol^{-1}. These H-bonds correspond to the shift of charge from the occupied orbital on oxygen to the H-bonding bonding region.

Electronic property analysis

The nature of the H-bonding interaction can be characterized from the topological analysis of electron density. According to the AIM theory [36, 37], the electron density ρ can represent the bond strength. A stronger bond is associated with a larger ρ value. The Laplacian $\nabla^2\rho$ value is generally used to reflect the characteristic of bond. The negative $\nabla^2\rho$ means the interatomic bond exists as the covalent bond, while the positive $\nabla^2\rho$ indicates that the bond belongs to ionic, hydrogen bonding, or van der Waals interactions. The $\nabla^2\rho$ value can be described by the sum of the three eigenvalues of the Hessian matrix of ρ ($\nabla^2\rho=\lambda_1+\lambda_2+\lambda_3$). When the two eigenvalues are negative and the third is positive, it is called the bond critical point. Three AIM criteria was proposed by Lipkowski et al. [58] to characterize the existence of H-bond, that is, 1) there is a bond critical point, 2) the electron density ρ and its Laplacian $\nabla^2\rho$ should be within the ranges 0.002-0.035 and 0.024-0.139 au, respectively.

As shown in Table 4, all of the topological parameters at the bond critical points, except those in bold, fall within the suggested value ranges, consequently, they can be classified as the hydrogen bonding interactions. In configurations F1, F2, and TF, the ρ values of the H-bonds involving C2-H6 are above 0.023 au. Therefore, the C2-H6 site on the imidazolium ring is the most favorable position to form H-bond, which has also been confirmed experimentally elsewhere [59, 60]. There possibly exists van der Waals interactions between $[Bmim]^+$ cation and $[PMoO]^{3-}$ anion in the four configurations F1, F2, F3, and TF. For example, in configuration F2 (Table 4), the low ρ values for C10-H16···O11, C11-H18···O2, C12-H20···O8 are 0.0052, 0.0066, 0.0055, respectively, which agree with the suggested criterion (~10^{-3} au) of van der Waals complexes [61, 62].

The difference of electron density for configuration F2 is shown in Fig. 4, which is obtained by subtracting the electronic density of each fragment from the total electronic density of configuration F2. The redistribution of the electron density is mainly in regions along the H-bond axes, where the electron density reduction is concentrated at the positions of H-bond donors. The electron density increase is observed at the H-bond acceptors. These features are consistent with those H-bonded configurations reported previously [63, 64]. The maps of electron density difference for other configurations are similarly observed in Fig. S2 in the electronic supplementary material. The kind of difference of electron density can also described by the Voronoi deformation density (VDD) charge analysis for the isolated cation and the cation moiety in each ion pair (Table S2). This VDD charge shows that the cation moieties have an increase in the net negative charge, confirming an electron transfer from the anion moiety to the cation moiety during the combination of the ion-pair. In particular, it was observed that the partial π electron show a transfer along the imidazolium ring from the C2-H6 group to the back-side C4(H7)-C5(H8) region. This behavior is consistent with the result of the difference of electron density (Fig. 4).

In the NBO analysis, the second-order interaction energy $E^{(2)}$ between the donor orbital i and the acceptor orbital j could

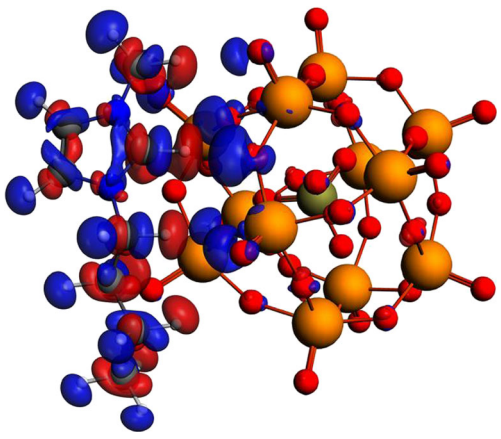

Fig. 4 Electron density difference map for configuration F2. The blue and red regions represent increased electron density and decreased electron density, respectively. The isodensity contours are 0.0015 electron bohr^{-3}

Table 5 The second-order interaction energies (in kcal mol^{-1}) and the total amount of electron transfer (in e) from the anion to cation on the basis of the NBO analysis

Ion pairs	Donor(i)[a]	Acceptor(j)[a]		charge transfer
T1	LP(O4)	σ*(C2-H6)	2.92	−0.0458
T2	LP(O1)	σ*(C13-H25)	0.69	−0.0408
F1	LP(O4)	σ*(C2-H6)	7.95	−0.0557
	LP(O9)	σ*(C9-H14)	2.54	
F2	LP(O4)	σ*(C2-H6)	12.24	−0.0748
F3	LP(O7)	σ*(C13-H25)	0.81	−0.0361
TF	LP(O2)	σ*(C2-H6)	1.67	−0.0609
	LP(O6)	σ*(C13-H24)	1.33	
	LP(O10)	σ*(C12-H20)	1.31	
	LP(O4)	π*(C2-N3)	3.89	

[a] LP denotes the lone pair orbital. σ* and π* represent anti-bond orbitals

be estimated by the equation, $E^{(2)}=\Delta E_{ij}=q_i\times F(i,j)^2/(\varepsilon_j-\varepsilon_i)$, where q_i is the donor orbital occupancy; ε_j and ε_i are diagonal elements (orbital energies) and $F(i,j)$ is the off diagonal NBO Fock matrix element.

The second-order orbital interaction energy $E^{(2)}$ and the charge transfer between the $[Bmim]^+$ cation and the $[PMoO]^{3-}$ anion are listed in Table 5. In configurations T1, F1, F2, and TF, the $E^{(2)}$ values of LP (O)→σ*(C2-H6) are larger than the others, reflecting the strong orbital interaction in the H-bonds involving the C2-H6 group. Especially, the largest $E^{(2)}$ value (~12 kcal mol^{-1}) corresponds to the strongest H-bond (C2-H6···O4) in configuration F2. For configurations T2 and F3, the $E^{(2)}$ value of LP (O)→σ*(C2-H6) is too small to list, which is in agreement with their small red shifts of the C2-H6 stretching vibration. The $E^{(2)}$ value of LP (O9)→σ*(C9-H14) in configuration F1 is 2.54 kcal mol^{-1}, while the $E^{(2)}$ values of the other bonds are about 1 kcal mol^{-1}. They are consistent with the trend of the H-bond strength. In configuration TF, the $p-\pi$ interaction LP (O4)→π*(C2-N3) with the value of $E^{(2)}$ (3.89 kcal mol^{-1}) was observed, which is attributed to its specific geometry. The charge transfer from the $[PMoO]^{3-}$ anion to the $[Bmim]^+$ cation has also been observed. Configuration F2 has the largest charge transfer (~0.075e), configurations F1 and TF have similar charge transfer, and F3 has the smallest one (0.036e). The charge transfer for each configuration does not have a direct relationship with the stability of the ion pairs. However, the charge transfer in the ion pairs may affect the electronic properties of the $[PMoO]^{3-}$ anion [15].

In the NCI approach, RDG was computed by the equation [39] $RDG=1/(2(3\pi^2)^{1/3})|\nabla\rho|/\rho^{4/3}$. In this approach, the plot of RDG vs. sign $(\lambda_2)\rho$ (the electron density multiplied by the sign of the second Hessian eigenvalue) can be used to distinguish the interaction nature between the $[PMoO]^{3-}$ anion and the $[Bmim]^+$ cation. Multiwfn 3.2 [65] was used to obtain the graph of RDG versus sign (λ_2) ρ and the RDG isosurfaces for the optimized structures of ion pairs. As shown Fig. 5a, for configuration F2, several obvious spikes are observed in the low-density and low-gradient region, suggesting the existence of the non-covalent interactions between the $[Bmim]^+$ cation and the $[PMoO]^{3-}$ anion. The low-density, low-gradient spikes at negative values signify again the H-bond existence between the ions. Finally, the low-density, low-gradient spikes very near zero correspond to the weak dispersion interaction.

Moreover, the gradient isosurfaces of RDG (=0.5), subject to the constraint of low density, is able to provide further visual information of non-covalent interactions in the corresponding space. According to the values of sign (λ_2) ρ, as shown in Fig. 5b, the blue or green isosurfaces indicate the formation of H-bonds between the hydrogen donor and the oxygen acceptor, corresponding to the negative spikes in Fig. 5a. The regions with the pistazinus (yellow-green) color show weak dispersion interactions. The plots of RDG versus

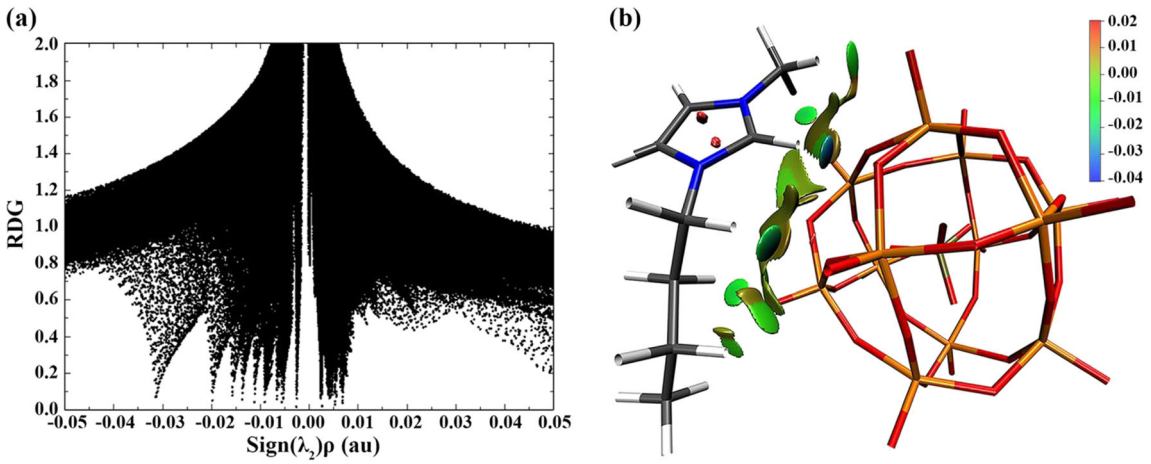

Fig. 5 The NCI analysis for configuration F2. (**a**) Plots of RDG versus the sign $(\lambda_2)\rho$. (**b**) RDG isosurfaces (RDG =0.5). Blue and red indicate dispersion interactions and strong nonbonded overlap, respectively

sign (λ_2)ρ and the RDG isosurfaces for the rest configurations are given in Fig. S3 and Fig. S4, respectively, in the electronic supplementary material. The $p-\pi$ interaction in configuration TF could also be observed, which has already been confirmed by the NBO analysis.

Conclusions

In this work, the interaction of novel POM-based ILs, composed of $[Bmim]^+$ and $[PMoO]^{3-}$, have been investigated employing the DFT computation. The geometrical characteristics, energetic properties, IR spectra, and the intermolecular H-bond characters between the $[PMoO]^{3-}$ anion and the $[Bmim]^+$ cation have been systematically analyzed and discussed. All the stable geometries of the ion pairs were characterized by multiple H-bonds with the type of C-H⋯O. The C2-H6 attached to the imidazolium ring is found to be the favorable position to form the H-bonds between the ion pairs. According to the interaction energy, the ion pairs formed between the $[PMoO]^{3-}$ and the $[Bmim]^+$ in the F region are more stable than those in T region.

The computed IR spectra demonstrate four types of Keggin-structured featured bands in the $[PMoO]^{3-}$ anion, which are in good agreement with the experimental result. The vibrational modes from isolated ion to ion pairs almost remain the same, implying the high structural stability of the $[PMoO]^{3-}$ anion. The red shifts of H-bond involving C2-H6 for all configurations were also observed, which can be assigned as the effect of H-bond. The interaction between the $[PMoO]^{3-}$ anion and the $[Bmim]^+$ cation has been comprehensively characterized by the electron density and its derivatives in the AIM scheme. The natural bond orbital analysis and the non-covalent interaction approach reveal the charge transfer from the anion to the cation. The obtained results are expected to provide an understanding of the interaction between the $[PMoO]^{3-}$ anion and the $[Bmim]^+$ cation and they will be beneficial for further designing new POM-based ionic liquids.

Acknowledgments This work was supported by the National Natural Science Foundation of China under Grants 21136005, and A Project Funded by the Priority Academic Program Development of Jiangsu Higher Education Institutions (PAAD).

References

1. Obi EI, Leavitt CM, Raston PL, Moradi CP, Flynn SD, Vaghjiani GL, Boatz JA, Chambreau SD, Douberly GE (2013) J Phys Chem A 117(37):9047–9056
2. Castner EW, Wishart JF (2010) J Chem Phys 132(12):120901
3. Chiappe C, Malvaldi M (2010) Phys Chem Chem Phys 12(37): 11191–11196
4. Hallett JP, Welton T (2011) Chem Rev 111(5):3508–3576
5. Huo C, Chan TH (2010) Chem Soc Rev 39(8):2977–3006
6. Li H, Bhadury PS, Song B, Yang S (2012) RSC Advances 2(33): 12525–12551
7. Zhang Z, Dong K, Zhao ZK (2011) ChemSusChem 4(1):112–118
8. Neumann R (2010) Inorg Chem 49(8):3594–3601
9. Long DL, Tsunashima R, Cronin L (2010) Angew Chem Int Edit 49(10):1736–1758
10. Leng Y, Wang J, Zhu D, Ren X, Ge H, Shen L (2009) Angew Chem 121(1):174–177
11. Li H, Qiao Y, Hua L, Hou Z, Feng B, Pan Z, Hu Y, Wang X, Zhao X, Yu Y (2010) Chem Cat Chem 2(9):1165–1170
12. Zhang X, Mao D, Leng Y, Zhou Y, Wang J (2012) Catal Lett 143(2): 193–199
13. Jing L, Shi J, Zhang F, Zhong Y, Zhu W (2013) Ind Eng Chem Res 52(30):10095–10104
14. Zhao P, Wang J, Chen G, Zhou Y, Huang J (2013) Catal Sci Technol 3(5):1394
15. Zhao P, Zhang M, Wu Y, Wang J (2012) Ind Eng Chem Res 51(19): 6641–6647
16. Zhu W, Wu P, Chao Y, Li H, Zou F, Xun S, Zhu F, Zhao Z (2013) Ind Eng Chem Res 52(49):17399–17406
17. Zhu W, Huang W, Li H, Zhang M, Jiang W, Chen G, Han C (2011) Fuel Process Technol 92(10):1842–1848
18. Chen DY, Sahasrabudhe A, Wang P, Dasgupta A, Yuan RX, Roy S (2013) Dalton Trans 42(29):10587–10596
19. Hasenknopf B, Micoine K, Lacote E, Thorimbert S, Malacria M, Thouvenot R (2008) Eur J Inorg Chem 2008(32):5001–5013
20. Wasserscheid P, Keim W (2000) Angew Chem Int Edit 39(21):3772–3789
21. Chaumount A, Wipff G (2008) Phys Chem Chem Phys 10:6940–6953
22. Li H, Lu Y, Wu W, Liu Y, Peng C, Liu H, Zhu W (2013) Phys Chem Chem Phys 15(12):4405–4414
23. Gao H, Zhang Y, Wang H-J, Liu J, Chen J (2010) J Phys Chem A 114(37):10243–10252
24. Dong K, Song Y, Liu X, Cheng W, Yao X, Zhang S (2012) J Phys Chem B 116(3):1007–1017
25. Izgorodina EI, MacFarlane DR (2011) J Phys Chem B 115(49): 14659–14667
26. Zhao X, Xing H, Yang Q, Li R, Su B, Bao Z, Yang Y, Ren Q (2012) J Phys Chem B 116(13):3944–3953
27. Turner EA, Pye CC, Singer RD (2003) J Phys Chem A 107(13): 2277–2288
28. te Velde G, Bickelhaupt FM, Baerends EJ, Guerra CF, Van Gisbergen SJA, Snijders JG, Ziegler T (2001) J Comput Chem 22(9):931–967
29. Perdew JP, Burke K, Ernzerhof M (1996) Phys Rev Lett 77(18): 3865–3868
30. Grimme S, Antony J, Ehrlich S, Krieg H (2010) J Chem Phys 132(15):154104
31. Lopez X, Maestre JM, Bo C, Poblet J-M (2001) J Am Chem Soc 123(39):9571–9576
32. Maestre JM, Lopez X, Bo C, Poblet JM, Casan-Pastor N (2001) J Am Chem Soc 123(16):3749–3758
33. Lenthe EV, Baerends EJ, Snijders JG (1993) J Chem Phys 99(6): 4597–4610
34. van Lenthe E, Ehlers A, Baerends EJ (1999) J Chem Phys 110(18): 8943–8953
35. Boys SF, Bernardi F (1970) Mol Phys 19(4):553–566
36. Bader RFW (1991) Chem Rev 91(5):893–928
37. Bader RFW (2002) Atoms in molecules. In: encyclopedia of computational chemistry. Wiley, New York
38. Johnson ER, Keinan S, Mori-Sánchez P, Contreras-García J, Cohen AJ, Yang W (2010) J Am Chem Soc 132(18):6498–6506

39. Ranga Rao G, Rajkumar T, Varghese B (2009) Solid State Sci 11(1): 36–42
40. Guan W, Yan LK, Su ZM, Liu SX, Zhang M, Wang XH (2005) Inorg Chem 44(1):100–107
41. Feng N, Zheng A, Huang S-J, Zhang H, Yu N, Yang C-Y, Liu S-B, Deng F (2010) J Phys Chem C 114(36):15464–15472
42. Bondi A (1964) J Phys Chem 68(3):441–451
43. Desiraju GR, Steiner T (2001) The weak hydrogen bond: in structural chemistry and biology, vol 9. Oxford University Press, Oxford
44. Shakourian-Fard M, Fattahi A, Bayat A (2012) J Phys Chem A 116(22):5436–5444
45. Angelina EL, Peruchena NM (2011) J Phys Chem A 115(18):4701–4710
46. Steiner T (2002) Angew Chem Int Ed 41(1):48–76
47. Mohajeri A, Ashrafi A (2011) J Phys Chem A 115(24):6589–6593
48. Gao Y, Zhang LQ, Wang Y, Li HR (2010) J Phys Chem B 114(8): 2828–2833
49. Dong K, Zhang S, Wang D, Yao X (2006) J Phys Chem A 110(31): 9775–9782
50. Ziegler T, Rauk A (1979) Inorg Chem 18(6):1558–1565
51. Ziegler T, Rauk A (1979) Inorg Chem 18(7):1755–1759
52. Morokuma K (1971) J Chem Phys 55(3):1236–1244
53. Rickert PG, Antonio MR, Firestone MA, Kubatko KA, Szreder T, Wishart JF, Dietz ML (2007) J Phys Chem B 111(18):4685–4692
54. Reichert WM, Holbrey JD, Swatloski RP, Gutowski KE, Visser AE, Nieuwenhuyzen M, Seddon KR, Rogers RD (2007) Cryst Growth Des 7(6):1106–1114
55. Mitoraj MP, Michalak A, Ziegler T (2009) J Chem Theory Comput 5(4):962–975
56. Mitoraj M, Michalak A (2007) J Mol Model 13(2):347–355
57. Lipkowski P, Grabowski SJ, Robinson TL, Leszczynski J (2004) J Phys Chem A 108(49):10865–10872
58. Köddermann T, Wertz C, Heintz A, Ludwig R (2006) Chem Phys Chem 7(9):1944–1949
59. Holbrey JD, Reichert WM, Nieuwenhuyzen M, Johnson S, Seddon KR, Rogers RD (2003) Chem Commun (14):1636–1637
60. Zhou P-P, Qiu W-Y (2009) J Phys Chem A 113(38):10306–10320
61. Bone RG, Bader RF (1996) J Phys Chem 100(26):10892–10911
62. Gora RW, Grabowski SJ, Leszczynski J (2005) J Phys Chem A 109(29):6397–6405
63. Torrent-Sucarrat M, Anglada JM (2006) J Phys Chem A 110(31): 9718–9726
64. Lu T, Chen F (2012) J Comput Chem 33(5):580–592